HIGH BURNUP FUEL TECHNOLOGY IN KOREA

KUN WOO SONG*, YONG HWAN JEONG, KEON SIK KIM, JE GEON BANG, TAE HYUN CHUN, HYUNG KYU KIM and KEE NAM SONG
Korea Atomic Energy Research Institute
1045 Daedeokdaero, Yuseong-Gu, Daejeon 305-353, Korea
*Corresponding author. E-mail : kwsong@kaeri.re.kr

Received January 29, 2008

High burn-up fuel technology has been developed through a national R&D program, which covers key technology areas such as claddings, UO_2 pellets, spacer grids, performance code, and fuel assembly tests. New cladding alloys were developed through alloy designs, tube fabrication, out-of-pile test and in-reactor test. The new Zr-Nb tubes are found to be much better in their corrosion resistance and creep strength than the Zircaloy-4 tube, owing to an optimized composition and heat treatment of the new Zr-Nb alloys. A new fabrication technology for large grain UO_2 pellets was developed using various uranium oxide seeds and a micro-doping of Al. The uranium oxide seeds, which were added to UO_2 powder, were prepared by oxidizing and heat-treating scrap UO_2 pellets. A UO_2 pellet containing tungsten channels was fabricated for a thermal conductivity enhancement. For the fuel performance analysis, new high burnup models were developed and implemented in a code. This code was verified by an international database and our own database. The developed spacer grid has two features of contoured contact spring and hybrid mixing vanes. Mechanical and hydraulic tests showed that the spacer grid is superior in its rod-supporting, wear resistance and CHF performance. Finally, fuel assembly test technology was also developed. Facilities for mechanical and thermal hydraulic tests were constructed and are now in operation. Several achievements are to be utilized soon by the Korea Nuclear Fuel and thereby contribute to the economy and safety of PWR fuel in Korea

KEYWORDS : High Burn-up Fuel, Cladding, UO_2 Pellet, Spacer Grid, Fuel Performance, Assembly Test

1. INTRODUCTION

During a decade from the mid 1980s to the mid 1990s, Korea Atomic Energy Research Institute (KAERI) developed fuel design technology for all PWR fuel types in Korea. After a successful completion, the design technology was transferred to the Korea Nuclear Fuel Company, the sole fuel vendor in Korea. As a result, the PWR fuel technology has been established in Korea. Then, KAERI launched a R&D program for developing self-reliant advanced fuel technology, which should enhance a fuel's reliability and economy.

The advanced PWR fuel, which we have focused on, is a high burn-up fuel since it can reduce the fuel cycle cost and the amount of spent fuel. A high burn-up fuel has been studied world-wide for the purpose of solving or relaxing the anticipated concerns at high burn-up such as a cladding corrosion, a fission gas release, and so on. As a result, it is known that new Zr-Nb alloys are more resistant to a corrosion and large grain UO_2 pellets are capable of decreasing the fission gas release rate. In addition, new spacer grids have been studied in order to protect fuel rods from a fretting failure and to increase the thermal margin.

To keep up with the state-of-the art for a high burn-up fuel, the R&D topics of KAERI consists essentially of the development of high corrosion-resistant cladding alloys, large grain UO_2 pellets, fuel performance analysis code, and high performance grids. In parallel with the above developments, fundamental studies have been carried out on a fuel performance database and fuel assembly tests. Significant progress has been made during the last 10 years (1997-2006). The achievements of each area are described below. A summary of the R&D areas is shown in Table 1.

2. DEVELOPMENT OF NEW CLADDING "HANA™"

2.1 Basic Research for New Zirconium Alloy Designs

The development of an advanced cladding has been considered as essential for achieving a high burn-up nuclear fuel. We have carried out a research program for the development of advanced Zr alloy claddings in order to meet the global demand for an extension of a fuel discharge burn-up to above 70 MWD/kgU. A great number of parameter studies [1-5] have been performed

Table 1. Summary of PWR Fuel R&D

	Activities	Achievements
Cladding	Alloy design, cladding fabrication, lab & in-rector test	HANA claddings
Fuel Pellet	Fabrication method, in-reactor test	Large-grain UO_2 pellet
Performance Analysis	Model & code development, PIE test	INFRA code
Spacer Grid	Shape design, grid fabrication, mechanical & thermal hydraulic test	Theta spring & hybrid mixing vane
Test facility	Construction of full size FA mechanical & thermal-hydraulic test	FAMect, HTL

to develop advanced Zr-based alloys for high burn-up fuel claddings. The effects of alloying elements and a heat treatment on the corrosion and the mechanical properties of Zr alloys were investigated systematically. Especially, Nb-containing Zr alloys were characterized to determine the optimum composition and heat-treatment conditions for an improvement of their corrosion resistance. The creep properties were also evaluated for the Nb-containing Zr alloys which were subjected to different heat treatments.

2.2 Fabrication of HANA Cladding

We have fabricated 6 kinds of advanced Zr alloy claddings named HANA (High performance Alloy for Nuclear Application) on the basis of the extensive basic researches. Each cladding was subjected to more than 10 different annealing conditions to optimize the heat treatment condition for improved properties. The fabricated HANA claddings were subjected to a variety of out-of-pile tests including corrosion, creep and LOCA tests as well as in-pile tests in the Halden research reactor.

2.3 Out-Of-Pile Properties

2.3.1 Corrosion Properties

The corrosion behavior of the HANA alloys whose chemical compositions are shown in Table 2 was evaluated in various corrosion environments by measuring the weight gain with the exposure time. Figure 1 shows the corrosion behavior of the HANA claddings in a 360°C 18.6MPa PWR-simulating loop system containing 2.2 ppm Li and 650 ppm B. All the HANA claddings showed a lower corrosion rate than Zircaloy-4, regardless of the alloy composition, and HANA-6 showed the lowest corrosion rate among the HANA claddings. It was also found that the corrosion resistance of the HANA claddings was highly dependent on the heat treatment condition in the manufacturing process and that a final annealing at a lower temperature is more desirable for the improvement of the corrosion resistance. The microstructure observation revealed that the precipitate size in the HANA claddings was finer than that in Zricaoly-4, which was considered to be one of the main reasons for a better corrosion resistance of the HANA claddings. The optimum corrosion performance of the Nb-containing Zr alloys was achieved when the fine second phase particles were uniformly precipitated in the matrix [6-7]. This implies that the precipitates play an important role in the corrosion behavior of a Nb-containing Zr alloy and that the precipitation of fine precipitates is crucial for obtaining the optimum microstructure for an improved corrosion resistance.

Table 2. Chemical Compositions of Zr Alloys Used in This Study

Alloy	Chemical composition (wt.%)
HANA-3	Zr-1.5Nb-0.4Sn-0.1Fe-0.1Cu
HANA-4	Zr-1.5Nb-0.4Sn-0.2Fe-0.1Cr
HANA-5	Zr-0.4Nb-0.8Sn-0.35Fe-0.15Cr-0.1Cu
HANA-6	Zr-1.1Nb-0.05Cu
Zircaloy-4	Zr-1.3Sn-0.2Fe-0.1Cr

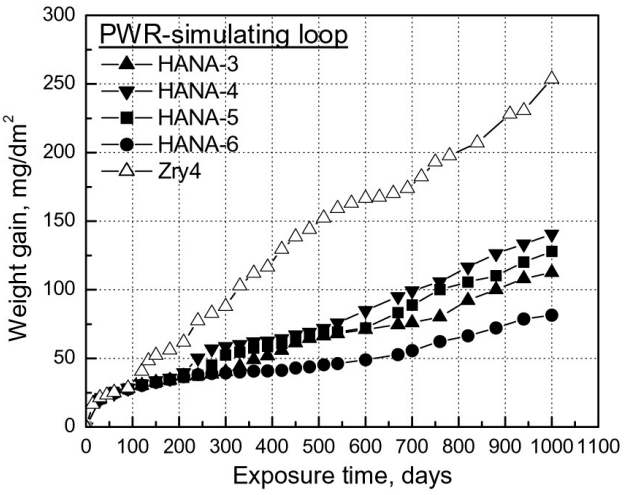

Fig. 1. Corrosion Behavior of HANA Claddings in a PWR-Simulating Loop Containing 2.2ppm Li and 650ppm B

2.3.2 Creep Properties

A thermal creep test was performed to evaluate the out-of-pile creep properties of the HANA claddings. Internal pressurization test was carried out, which was designed to create a hoop stress between 100 and 150MPa at the test temperature by an injection of Ar gas. Figure 2 shows the diametral strain of the HANA claddings which were heat treated at 510°C. Each cladding shows a steady state secondary creep behavior after 75 days, where the HANA claddings showed a lower creep rate than Zircaloy-4. From the results of a thermal creep test of the HANA claddings, it was found that an optimization of the final heat treatment temperature as well as the alloying elements is crucial for an improvement of the creep resistance.

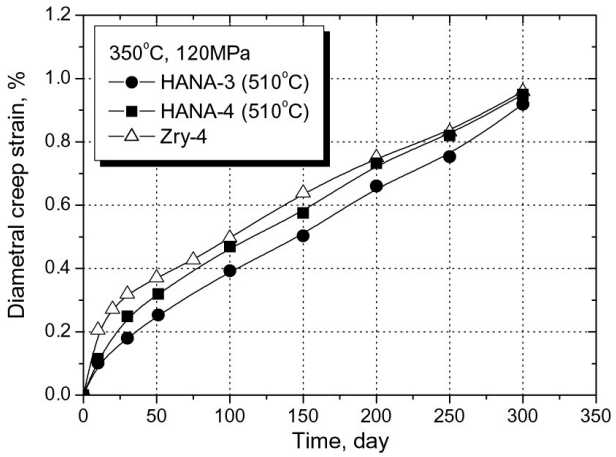

Fig. 2. Thermal Creep Properties of the HANA Claddings

2.3.3 LOCA Properties

Thermomechanical test to simulate the initial stage of a LOCA (Loss of coolant Accident) was conducted, where the pressurized cladding was heated at a rate of 1, 10 and 100°C per second until a rupture. Figure 3 shows the burst elongation with the temperature of the HANA claddings subjected to a final annealing at 470°C as well as the as-received Zircaloy-4 after a thermomechanical test [8]. Burst elongation of the Zircaloy-4 showed two peaks at 800°C and 1100°C, which can be closely related to a phase transformation of the Zr alloys [9]. The deformation behavior of the HANA claddings was similar to that of Zircaloy-4. However, the recovery of the elongation started at a lower temperature when comprared to Zircaloy-4, which resulted from an expansion of the phase transformation by a Nb addition.

Thermal quench test was performed, in which the specimen had been oxidized in a flowing steam at a desired temperature up to 1200°C and then quenched by water. The threshold ECR (Equivalent Cladding Reacted) of each cladding was evaluated. Figure 4 shows the failure map of the thermally quenched Zircaloy-4 and the HANA claddings after a subsequent high temperature oxidation [8]. An open symbol represents a specimen that remains sound after a water quenching. A closed symbol represents a specimen that failed. Threshold ECR value of the HANA claddings was higher than the conventional value of 17%

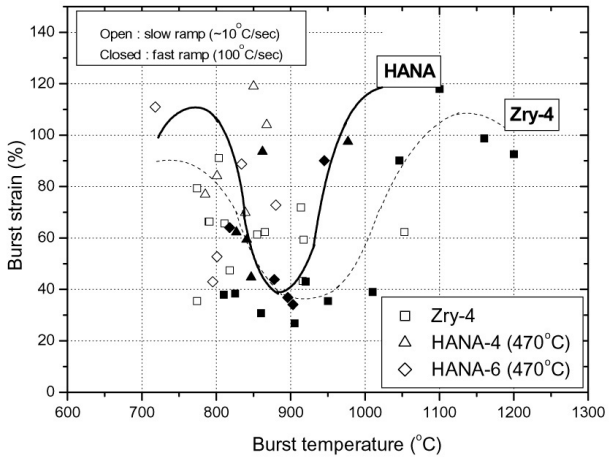

Fig. 3. Thermomechanical Test Results of the HANA Claddings and Zircaloy-4[8]. Open and Closed Symbol Represents Slow (=~10°C/sec) and Fast Thermal Ramp (=100°C/sec), Respectively

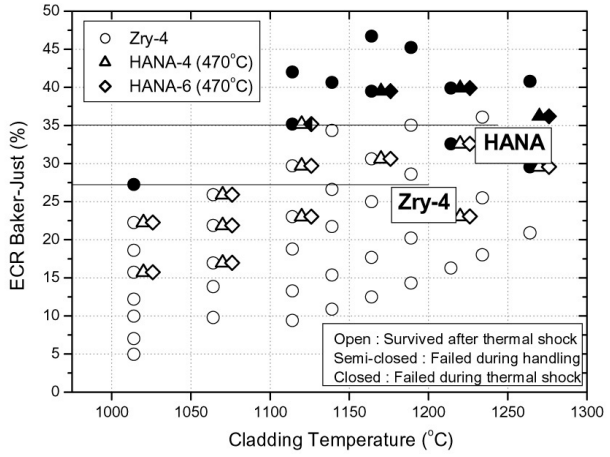

Fig. 4. Failure Map of the HANA Claddings with the Oxidation Temperature and ECR Value [8]

for Zircaloy-4, which is mainly due to the fact that the Nb decreases the oxidation rate as well as the hydrogen pickup rate .

2.4 In-Pile Test

The in-pile tests of the HANA claddings were performed in the Halden research reactor. The test rods manufactured by HANA claddings have been irradiated for about 536 full power days corresponding to about 32 MWD/kgU. The water chemistry, fluence and thermal hydraulic conditions were maintained similar to those of commercial PWRs during the irradiation test. The oxide thicknesses of the test rods ranged from 9 to 28μm depending on the alloy composition and axial position as shown in Fig. 5. The average oxide thickness for the highest heat flux region of each segment is also plotted in Fig. 5 for all the test rods. HANA claddings showed a better corrosion resistance than the reference cladding. The corrosion resistance of the HANA claddings was improved by 40~50% when compared to the reference cladding on the basis of the oxide thickness measurements. It was confirmed that all the HANA claddings had an excellent corrosion resistance in the in-reactor conditions as well as the out-of-pile conditions.

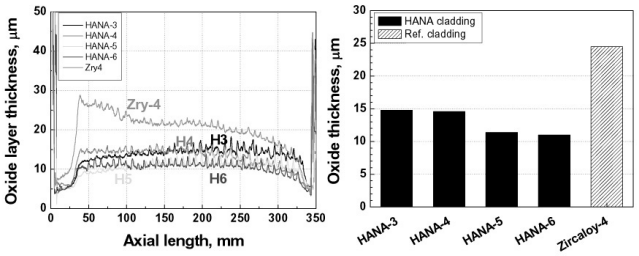

Fig. 5. In-Pile Corrosion Properties of HANA Claddings

3. DEVELOPMENT OF AN ADVANCED PWR FUEL PELLET

3.1 Large Grain UO_2 Pellet

Uranium dioxide fuel pellets which are widely used in light water reactors are manufactured by a conventional powder processing method [10]; UO_2 powder is pressed into green pellets and then sintered at 1700-1780 °C in a hydrogen-containing gas. The UO_2 pellet properties - density, pore structure, and grain size - greatly influence the in-reactor performance of the UO_2 pellet. Especially, the amount of fission gas released during an irradiation decreases as the grain size of the UO_2 pellets increases [11], and thus large-grain UO_2 pellets are desirable at a high burnup. A large-grain UO_2 pellet meets the restraint of the fission gas release which is one of the most important requirements for a high burn-up fuel.

The fabrication of large-grain UO_2 pellets has been investigated extensively, so many fabrication methods have been developed. The most prevailing method is simply to add sintering agents to UO_2 powder. Many sintering agents are known such as niobia [12,13], titania [14], chromia [15], and magnesia [16]. It is also known that the grain size of UO_2 pellets can be increased, without sintering agents, by using UO_2 powder with a high sintering activity [17]. Wood and Perkins [18] have reported that the addition of UO_2 seeds to UO_2 powder enhances the grain growth.

Our large-grain pellet was fabricated by using a specially heat-treated uranium oxide seed [19]. Figure 6 shows a schematic of the developed UO_2 pellet fabrication process. Developed technology has a good adaptability to the conventional fabrication process because it involves simply adding heat-treated uranium oxide seeds to UO_2 powder at an amount of less than 6 wt%.

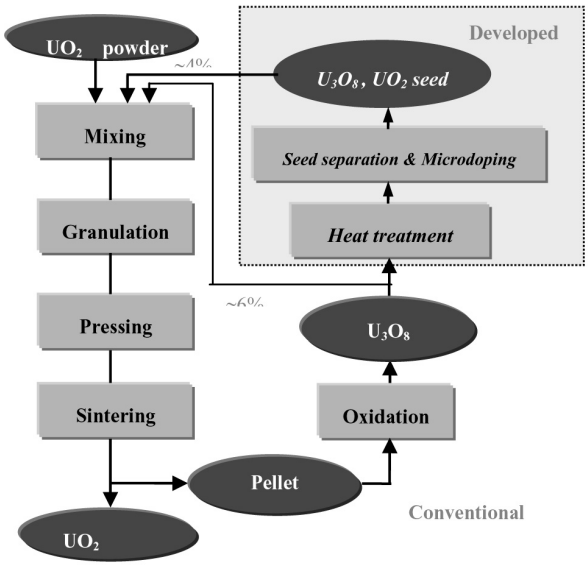

Fig. 6. Schematic of UO_2 Pellet Fabrication Process

The heat-treated uranium oxide seeds are U_3O_8 seeds, UO_2 seeds or activated U_3O_8, which are prepared by recycled pellet scrap. The conventionally recycled U_3O_8 powder is shown in Fig. 7(a), and various uranium oxide seeds are shown in Fig. 7(b)-7(d). When the recycled U_3O_8 powder was heat-treated at 1200-1500 °C for various times in a controlled atmosphere, the crystals constituting a U_3O_8 particle increased in size with the

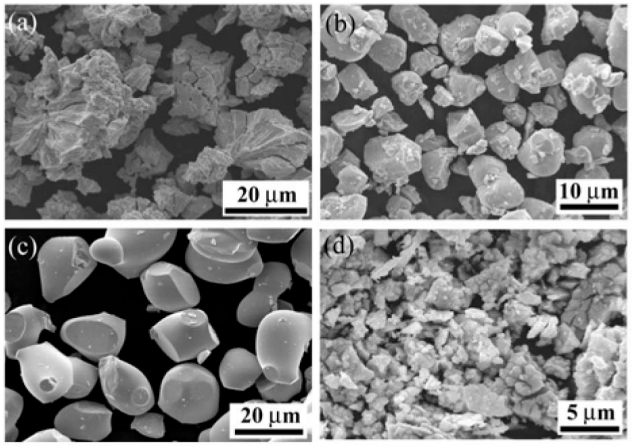

Fig. 7. Typical Shape of (a) Conventional U_3O_8, (b) U_3O_8 Seed, (c) UO_2 Seed and (d) Activated U_3O_8.

temperature. The seeds shown in Fig. 7(b) and Fig. 7(c) were made by a mechanical dividing process after the heat-treatment. The divided seeds had a polyhedron shape and were usually comprised of one grain. In a sintering process of the powder compact containing seeds, a large seed could enhance the grain growth by easily absorbing the surrounding small particles.

Activated U_3O_8 in Fig. 7(d) was made by a low temperature oxidation of a scrap pellet or a further oxidation of divided seeds. The size of an activated U_3O_8 is much smaller than that of the conventionally recycled U_3O_8. It has almost two times larger specific area than the conventionally recycled U_3O_8. Thus, it can be used as a seed without a density drop.

The uranium oxide seeds such as U_3O_8 seeds, UO_2 seeds, and activated U_3O_8, successfully act as a grain-growth promoter. The microstructures of a developed large-grain UO_2 pellet are shown in Fig. 8 and compared with that of the conventional UO_2 pellet. The grain size of the seeded or micro-doped pellets increases up to 14 μm from 8 μm. The content of a seed is usually less than 5 %. Aluminum is used as a dopant, and the doping level is controlled to below 100 ppm. We also developed a 25μm-grain-sized pellet by combining seeds with a micro-doping.

Thermal stability of a UO_2 pellet was improved by more than 30% for its density increment after a re-sintering test. Thus, the developed large-grain pellet reduces the fabrication cost as well as the fission gas release rate during an irradiation.

3.2 Burnable Absorber Fuel Pellet

For long cycle operation, a new burnable absorber fuel which improves the neutron economy by reducing the residual poison is required. One of the ways to meet the above need could be a duplex fuel pellet consisting of two distinct regions with different compositions; an outer annular shell and an inner cylindrical core. One is an annular shell composed of enriched UO_2-2%Er_2O_3 and the other is a cylindrical core composed of natural UO_2-(6-12)%Gd_2O_3. A schematic of a duplex pellet is shown in Fig. 9.

A nuclear analysis indicates that the duplex burnable absorber pellets are better in their neutronic performance than gadolinia pellets and could be applicable to an extended fuel cycle. From the viewpoint of a pellet fabrication process, however, a duplex structure may bring about a big concern because the inner portion and the outer region are composed of different materials. During the sintering process, different materials may

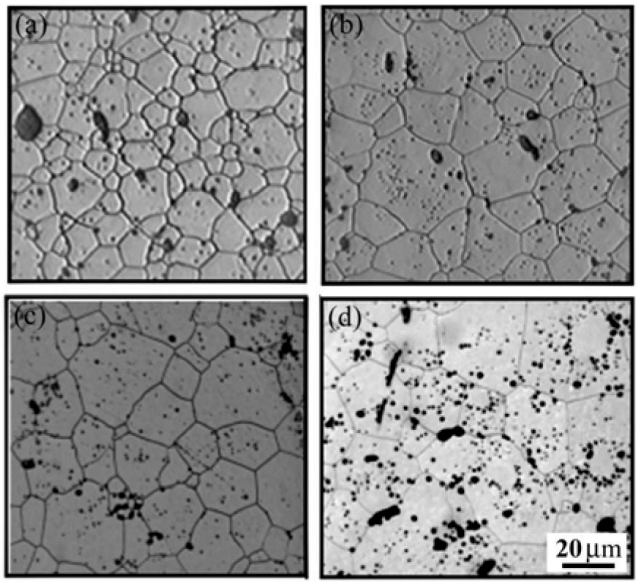

Fig. 8. Microstructures of (a) Conventional, (b) U_3O_8 Seeded, (c) Al-Microdoped and (d) Al-Microdoped Seed Added UO_2 Pellet

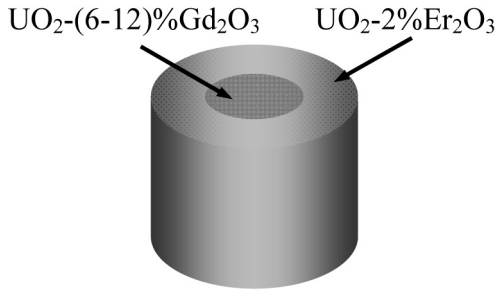

Fig. 9. Schematic of Duplex Burnable Absorber Pellet

cause a large difference in the densification rate between the inner cylindrical core and the outer annular shell, and thereby generate an undesirable internal stress at an interface between both portions (Fig. 10(a)). Crack-free bonding technique between a annulus and inner cylinder was developed by using a sintering agent such as MnO (Fig. 10(b)). It is reported that MnO sufficiently enhances the shrinkage rate of a intermediate sintering stage in the UO_2-Gd_2O_3 system [20].

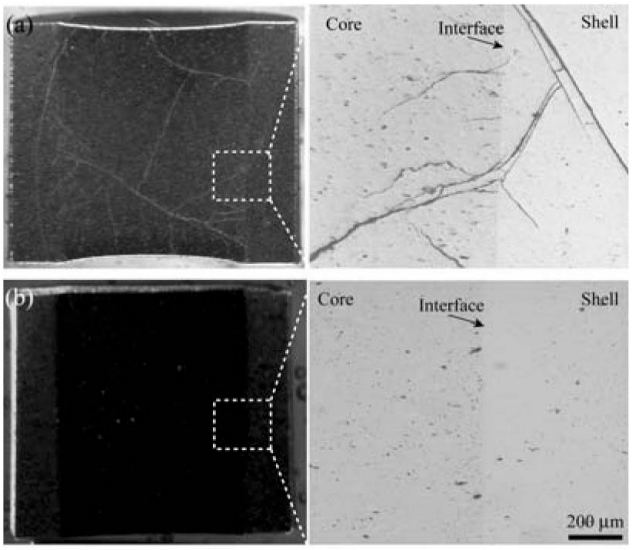

Fig. 10. Microstructures of (a) Conventional and (b) Developed Duplex Burnable Absorber Pellet

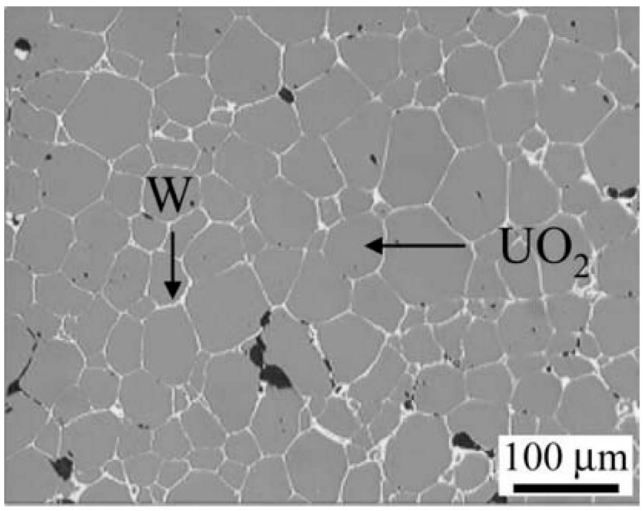

Fig. 11. UO_2 Pellet with a Continuous W Metal Channel

3.3 Cermet Fuel Pellet

In an effort for an the application to a next generation fuel pellet for a PWR, UO_2-Metal cermet fuel has been developed. In UO_2-Metal cermet fuel, the metal includes several high melting point metals such as W, Mo, Cr. A new fabrication process for UO_2-W cermet fuel has been developed in order to improve the thermal conductivity of a UO_2 pellet by the addition of a small amount of W. Figure 11 shows the microstructure of a UO_2-W cermet fuel with a continuous W channel enveloping UO_2 grains. It can be fabricated even with a small amount of a metal phase - below 6 vol.% and it shows an improved thermal diffusivity, about 50% higher than that of a pure UO_2 pellet [Fig. 12].

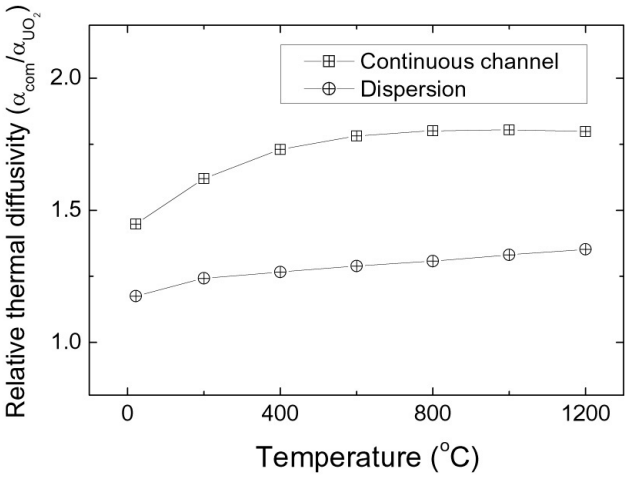

Fig. 12. Thermal Diffusivities of the UO_2 Pellet Containing Tungsten Channel or Tungsten Dispersion Relative to Pure UO_2 Pellet

4. HIGH BURNUP UO_2 FUEL ROD PERFORMANCE ANALYSIS

4.1 Development of a High Burnp UO_2 Fuel Rod Performance Analysis Code INFRA

A UO_2 fuel rod performance analysis code, INFRA (INtegrated Fuel Rod Analysis) was developed [21]. Various new models which can predict a high burnup effect up to a 70 MWd/kgU rod average burnup were incorporated and important models are listed below

- rim microstructure formation prediction model
- irradiated fuel thermal conductivity model including a rim region
- mechanistic fission gas release model
- finite element analysis module for PCMI analysis

For a verification of the INFRA code, various fuel performance database were used such as IFPE, HRP and domestic high burnup fuel PIE results and, from 2003 to 2006, the INFRA code participated in the FUMEX-II program which was managed by the IAEA for a verification of the high burnup fuel performance codes of the participants (~20 countries). The FUMEX-II verification results revealed an accurate prediction ability of the INFRA code when compared with other codes (Fig. 13 and Fig. 14) [22].

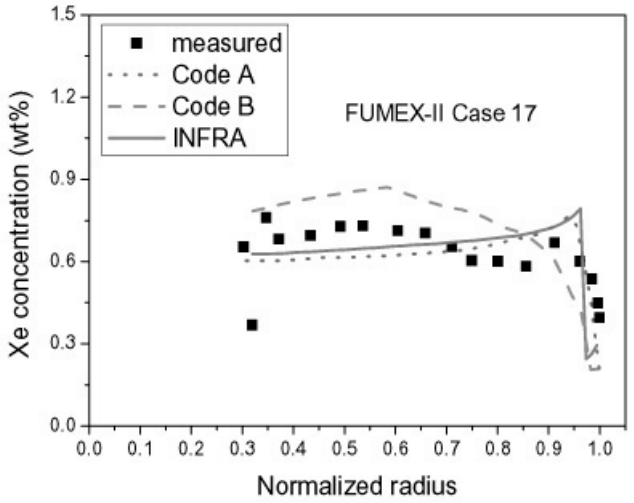

Fig. 13. Prediction of the Radial Xe Distribution

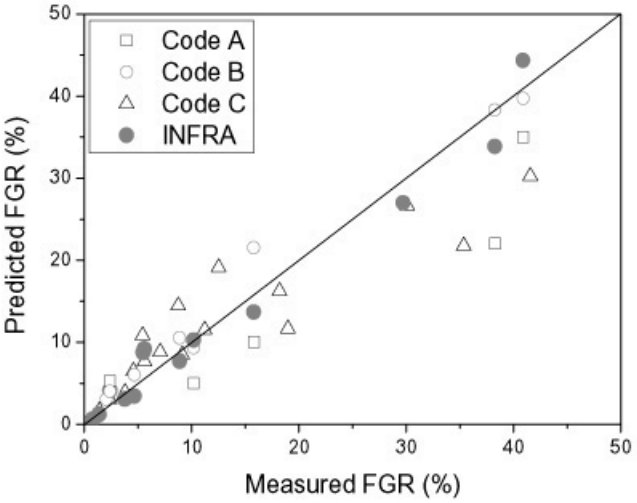

Fig. 14. Fission Gas Release Prediction Results

4.2 High Burnup UO_2 Fuel Performance Analysis

4.2.1 Post Irradiation Test of a High Burnup UO_2 Fuel

In order to investigate the behavior of a UO_2 fuel at a high burnup, a fuel assembly with the highest discharge burnup in Korea was selected and PIE was performed [23]. The fuel assembly burnup is 50.5 MWd/kgU and the peak rod average burnup (M04 rod) is 56.7 MWd/kgU. The post-irradiation examination of the fuel was performed by the procedure shown in Fig. 15. The highest burnup fuel rod M04 was transported to the hot cell for the non-destructive test and the destructive test.

Eddy current scanning of the fuel rod was performed to measure the fuel rod diameter and oxide layer thickness. Figure 16 shows the axial distribution of the oxide layer thickness measured by the eddy current and the oxide

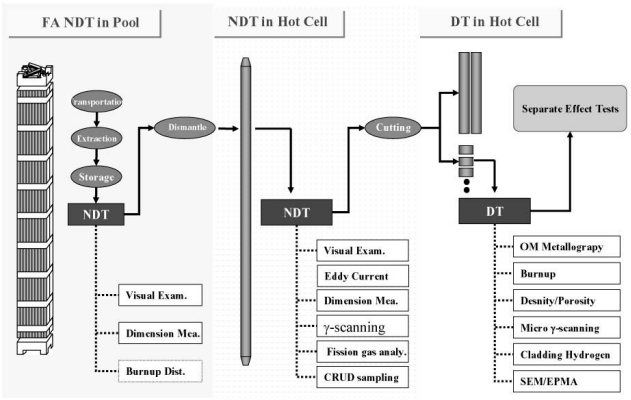

Fig. 15. Overall procedure of a PIE

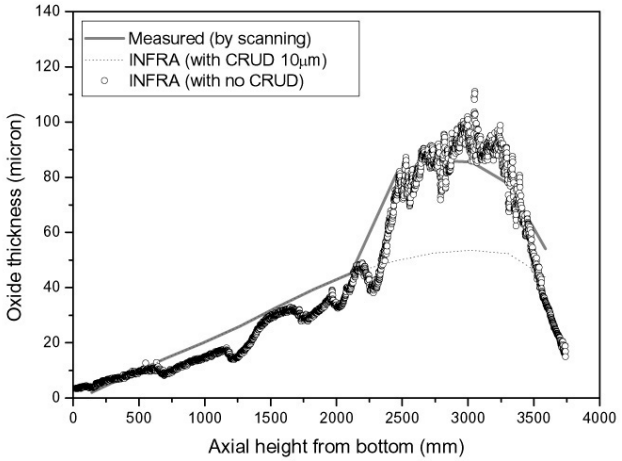

Fig. 16. Axial Distribution of the Oxide Layer Thickness

thickness predicted by INFRA. The peak oxide layer thickness was higher than 100 μm locally and correspondingly the peak hydrogen content in the cladding was higher than 500 ppm. Fission gas release rate was measured by a puncturing test and the collected gases were analyzed by QMS(Quadruple Mass Spectrometry). The fractional fission gas release rate was 4.9%.

For the destructive examination, the M04 fuel rod was cut at four different positions. Optical microscopy, SEM and EPMA were performed to examine the microstructure of the high burnup UO_2 fuel. By an optical microscopy of the fuel rod cross section, an extensive pellet cracking was observed in both the radial and axial directions, and after an etching of the UO_2 fuel, two different color regions were observed and the interface line coincided with the dish boundary. Figure 17 shows that there are more fission gas bubbles nucleated inside the UO_2 grain in the dark region. In the dish region, UO_2 can expand more freely than in the outer region. The outer region expansion may be restricted and compressive stresses exist which could hinder a nucleation of the fission gas bubbles. Stress analysis result showed a significant difference in the compressive stresses between the dish and outer regions.

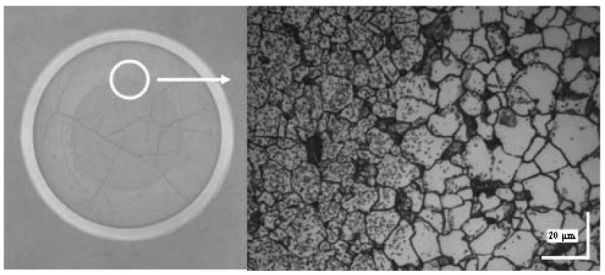

Fig. 17. Cross Section of a Fuel Rod After an Etching

By using the optical microscopy and SEM images, the pore and bubble size distributions in the UO_2 grain were analyzed. The average grain size of the UO_2 grains in the centre region was about 14.6 μm (Linear intercept method). Considering the as-fabricated grain size of 11 micron, a grain growth had occurred. The Nd distribution indicates the radial burnup distribution, and the Xe distribution indicates the rim microstructure formation. A low Xe concentration in the centre region may be due to the fission gas release during an irradiation. The rim microstructure can be easily observed easily by the etched OM result. Based upon OM, SEM and EPMA results, rim microstructure widths were estimated for a fully developed and transition region respectively.

4.2.2 Post Irradiation Annealing Test of a High Burnup UO_2 Pellet

In order to investigate the fission gas behavior during a temperature transient, PIA(Post Irradiation Annealing) apparatus was developed and installed at PIEF(Post Irradiation Examination Facility) in KAERI [24]. Figure 18 shows the PIA equipment installed in a hot cell. During the test, the specimen is swept by upward regulated gases (inert or air or oxygen) and mixed with released radioactive fission gases. The escaped gases from the furnace pass through filters to remove toxic fission gases. Filtered gases pass through a beta chamber for a beta counting and pass into the cold trap which is cooled by a liquid nitrogen supply system for a gamma counting. High purity Ge detector can count cumulative release values of the fission gases. For a detailed quantitative analysis, QMS system was installed in the glove box.

Some segments with a length of several centimeters were prepared for the PIA test. Specimen characteristics were analyzed by ORIGEN-S. For the inter-granular fission inventory measurement, a controlled oxidation technique was used. Prior to the main test, preliminary tests were performed to set the optimized test condition such as the temperature, heating rate, test time, etc. SEM image of a post-test specimen showed a grain boundary segregation by a controlled oxidation under a test condition. No additional release observed after 200 minutes which means the inter-granular fission gas inventory was evacuated. But as mentioned in previously reports [25], exact distinction of an inter or intra-granular fission gas inventory requires a measurement of Xe-132 which is generated by short a re-irradiation of a specimen.

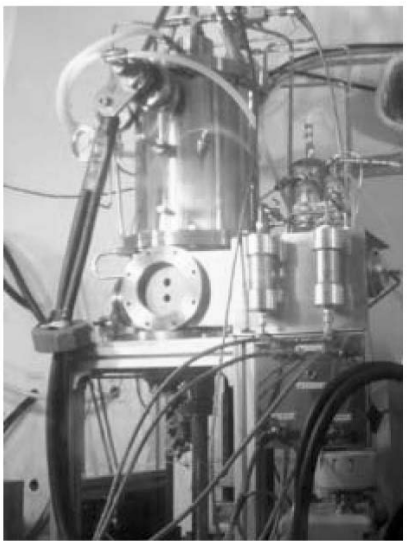

Fig. 18. PIA Apparatus in a Hot Cell

By considering the pre-test results, the PIA test was performed by using an irradiated high burnup UO_2 specimen. Figure 19 shows the Kr-85 release behavior during the PIA test. The intra-granular fission gas inventory was almost all released within 200 min at 500°C At this time, the temperature was increased up to 1400°C to extract the intra-granular fission gas inventory. After two hours of a holding time at 1400°C, the Kr-85 release was saturated and no additional fission gas release occurred, and after a few hours cooling, the temperature was re-increased up to 1400°C but an additional fission gas release was not detected. In fact, these oxidation and annealing techniques can't extract all the intra-granular fission gases, but most of the fission gases could be extracted. And, the remaining Kr-85 must be measured by additional examinations such as EPMA and a specimen melting.

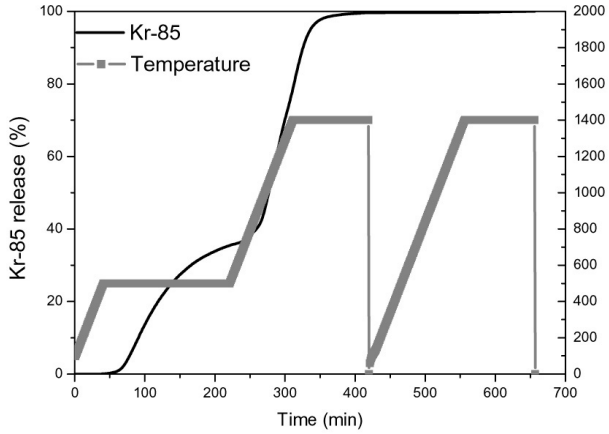

Fig. 19. Kr-85 Release Behavior During the PIA Test

By assuming all the Kr-85 was released, the inter-granular fission gas inventory was estimated at about 40% of the total fission gas inventory and it will be re-corrected by a re-irradiated specimen test result.

4.2.3 Mechanical Characteristic of High Burnup Fuel Cladding

To obtain the mechanical strength, the 0.2% offset YS(Yield Strength) and UTS(Ultimate Tensile Strength) were evaluated, and the UE(Uniform Elongation) and TE(Total Elongation) were also evaluated as a measure of a ductility. Figure 20 shows a comparison result of the mechanical strength and ductility of the irradiated Zircaloy-4 with the PROMETRA database. The values of the yield strength and ultimate tensile strength were almost similar regardless of the temperature, which is a reasonable result, when considering that all of the Zircaloy-4 claddings in this study and in the PROMETRA test program were irradiated for 3 cycles.

From the figure, it is confirmed that the 0.2% offset YS and the UTS abruptly decrease with an increasing temperature. The UTS was evaluated to be 942.7 MPa at RT, and 678.8 MPa at 400°C, but, it was abruptly diminished to 282.6 MPa at 600°C, which is achievable in the RIA condition. Especially, it decreases to 58.3 MPa at 800°C, an extreme condition, which corresponds to 6% of the UTS at room temperature. This means that the mechanical strength of the high burn-up Zircaloy-4 cladding sharply decreases in the RIA-relevant temperature range. And also it is shown that both the UE and TE increase with an increasing temperature. Especially, they abruptly increase at 600°C, but become lower beyond this temperature. This peculiar behavior was also observed in the PROMETRA program which is a mechanical property relevant test program in conjunction with the CABRI program for simulating a RIA [26]. It is believed that this behavior is caused by the minimum elongation phenomenon by dynamic strain aging of the Zircaly-4 cladding material beyond 600°C.

The stereoscope photographs of the specimens after the ring tensile test are shown in Fig. 21. Figure 21 represents the fracture patterns of the non-irradiated and high burn-up Zircaloy-4 cladding specimens. As shown in the figure, the fracture patterns such as a 45° shear type fracture were observed in the non-irradiated cladding at room temperature. On the contrary, the fracture pattern of the high burn-up Zircaloy-4 cladding showed completely different fracture

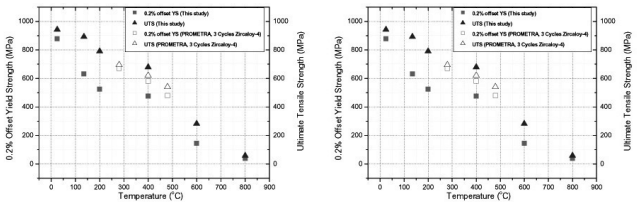

Fig. 20. Comparison of the Mechanical Strength and Ductility with the PROMETRA Database

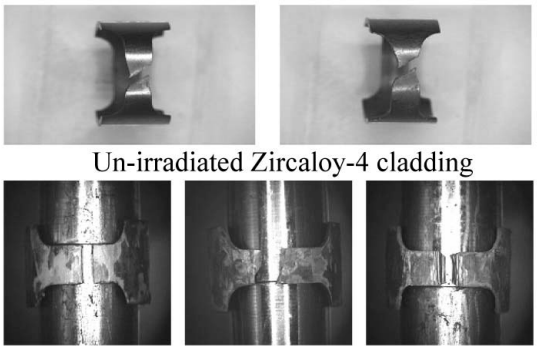

Fig. 21. Fracture Patterns After the Ring Tensile Tests

patterns from the non-irradiated Zircaloy-4 cladding. The fracture type was observed to be vertical in the tensile direction without a necking at all of the test temperatures, which is convincing evidence of the brittle fracture behavior of a high burn-up fuel cladding regardless of the temperature. This means that even at a high temperature, 600°C or 800°C, the fracture pattern showed a brittle fracture behavior. Accordingly, it was found that the high burn-up Zircaloy-4 cladding becomes very brittle even at the high temperatures achievable during a design-basis accident [27].

5. DEVELOPMENT OF ADVANCED SPACER GRID TECHNOLOGY

5.1 Description of Spacer Grid

Spacer grid is a major structural component of a nuclear fuel assembly requiring various design bases as well as a high performance. Advanced spacer grid technologies like springs and mixing vanes have been developed. One of the spacer grids with a Theta(θ) spring [28], as shown in Fig. 22, has a geometrical feature of a conformal contact shape at the support part of the fuel rods. The Theta spring was developed by a systematic design optimization to enhance its fuel rod support characteristics, based on a H-shape spring [29] in 1997. The other is the Doublet-type spacer grid [30] as also shown in Fig. 22. This spacer grid is also modified based on the initial Doublet-type spacer grid [31] of which the main feature is the support of a fuel rod with a long line contact. On the other hand, Hybrid Mixing Vanes were devised to enhance the thermal performance of a spacer grid. Those are a set of two different pairs of vanes of every junction of a spacer grid, which are designed to efficiently generate a large swirl flow in each subchannel center and cross flows between neighboring rod gaps, simultaneously. They are also made to decrease the hydraulic resistance from a smooth flow blocking by a inclined vane bending.

5.2 Out-of-pile Performance Tests and Results

Various out-of-file tests were conducted to investigate the performance of the new technologies for the advanced spacer grid as follows:

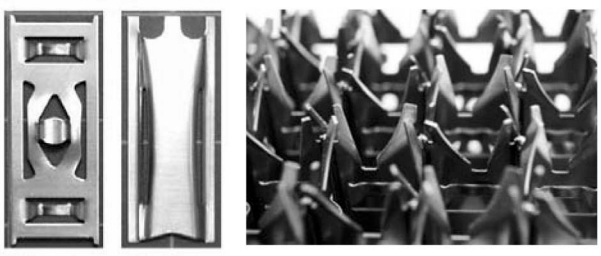

Fig. 22. Developed Springs and Hybrid Mixing Vanes

- Spring characteristics test
- Vibration characteristics test
- Fretting wear test
- Impact strength test
- Pressure drop test
- Critical heat flux test

5.2.1 Spring Characteristics Test

The force-deflection test was performed up to the plastic range. Plastic sets of the developed springs were measured when those were deflected up to 1.0 mm and unloaded. The spring with less plastic sets would make a loss of the spring force small, and consequently would be able to stably support the fuel rod. According to the test results [32], the measured plastic sets were comparatively smaller than the commercial springs

A contact area analysis was carried out by a finite element analysis using ABAQUS in order to simulate the contact area and shape between the fuel rod and the spring when the fuel rod is inserted into the spacer grid cell. According to the analysis results [32], the contact area of the Theta spring is gradually increasing up to a 0.4 mm deflection. Considering that the working range of the spring deflection when the fuel rod is loaded into the spacer grid cell is usually assumed to be around 0.3~0.4 mm, it turned out that the contact area of the Theta spring remains wide enough to support a fuel rod and to suppress the rod vibration.

5.2.2 Fuel Rod Vibration and Fretting Wear Characteristics

To investigate a fuel rod's support and vibration characteristics, a modal test of a single dummy fuel rod supported by five spacer grids has been performed in air at room temperature. The objective of this test was to compare the maximum deflection of each spacer grid shape when the same input force is applied to a fuel rod. According to the test results [32], the maximum deflections of a fuel rod for the springs are as follows; 0.08 mm for the Doublet spring, and 0.11 mm for the Theta spring. When the maximum deflections of a fuel rod are smaller, it means that the spacer grid has a better vibration resistance to external forces and this leads to a greater resistance to fretting wear damage.

Fretting wear test at a reactor operation temperature was performed at AECL of Canada in early 2004 to derive a fuel rod wear coefficient in the case of the theta spring. The test was carried out in water of 320°C and 10 MPa.

When the workrate model [33] was applied, the wear coefficient was evaluated as 113×10^{-15} Pa^{-1}. Although the wear test was not conducted for the doublet spring, it is anticipated that a lower wear coefficient would be obtained than the Theta spring's from the vibration result.

5.2.3 Spacer Grid Impact Strength

An impact strength test was performed by using a

pendulum type impact tester for a full size spacer grid with the Theta spring. In the beginning, the impact strength of the original spacer grid satisfied the 0.3 g seismic criterion with a narrow margin. Then, the dimensions and location of a dimple were modified recently by a systematic design optimization [34] to enhance the impact strength. It resulted in a 10% increase in the impact strength.

5.2.4 Pressure Drop Test

The pressure drop tests were performed with a 5x5 rod bundle with the spacer grids in Fig. 23. The straps of the spacer grids were fabricated to reduce the hydraulic resistance through a coining/chamfering. The tests were conducted at atmospheric pressure and temperature with water, whose the conditions cover a Reynolds number from 10^4 to 10^5. Pressure loss coefficients of the spacer grid were evaluated along with the Re number. From the results, it is 1.02 at $Re=10^5$ which is slightly lower than or comparable with conventional spacer grids.

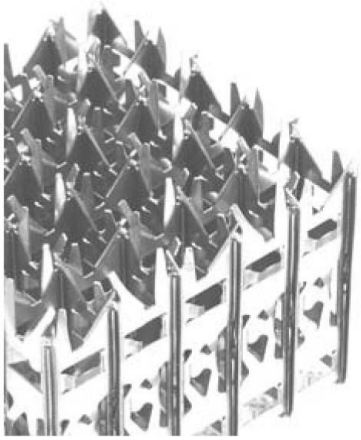

Fig. 23. 5x5 Spacer Grid with Theta Spring and Hybrid Mixing Vanes

5.2.5 Critical Heat Flux Test

The critical heat flux (CHF) test was also performed to quantify the enhancement due to the Hybrid Mixing vanes [35]. The CHF test was conducted with two 5x5 rod bundles; one is a rod bundle with Hydrid Mixing vanes, the other a rod bundle without a mixing vane. The rod bundle had a non-uniform radial power distribution and uniform axial power distribution with a gird span of 564 mm. The working fluid of this test was refrigerant R-134a. The test was performed in the ranges of the inlet pressure, P_{in} = 2000~3000 kPa, mass flux, G = 1500~3000 kg/m^{2}s, and inlet subcooling, h_{in}= 10~55 kJ/kg, which simulates the PWR operating conditions for a water equivalence through a fluid-to-fluid modeling.

The CHF enhancements were evaluated and defined as follows: $(q''_{MV} - q''_{NMV})/q''_{NMV} \times 100$. The average of the CHF values for the hybrid mixing grid for 20 data sets is 18.2% higher than those for the no vane grids. Consequently, the Hybrid Mixing vanes showed an excellent CHF performance.

6. DEVELOPMENT OF FUEL ASSEMBLY TESTERS

6.1 Fuel Assembly Mechanical Characterization Tester (FAMeCT)

6.1.1 Fuel Assembly Mechanical Test Items

Necessary items for fuel assembly mechanical tests are as listed below.

- Vibration test: the vibration test is conducted to obtain the vibration behaviour of a fuel assembly. It is a dynamic test to investigate a fundamental vibration characteristic of a fuel assembly. Natural frequencies, model shapes and critical damping ratios are the important outputs. These are used for the fuel assembly accident analysis under the condition of a seismic and LOCA.
- Stiffness test: this test is to basically examine the static response of a fuel assembly while it is loaded laterally as well as axially. As for the data, deflection at each grid location and strains of the guide thimbles are measured during a loading and unloading. The test result is used for verifying the fuel assembly model for the reactor analysis.
- Impact test: the purpose of this test is to find the fuel assembly performance subjected to the lateral and axial impact condition. Possible case of a fuel assembly impact is a banging of a fuel assembly against an adjacent one or a core baffle under the conditions of a seismic and LOCA. Integrity of the fuel assembly is the major concern under such an accident. Impact force, displacement and rebound height are measured.

To conduct these tests, a Fuel Assembly Mechanical Characterization Tester (FAMeCT) has been constructed, which is shown in Fig. 24.

6.1.2 Lateral Vibration Tests and Results

Full size of an advanced fuel assembly for a KSNP (Korea Standard Nuclear Power Plants) has been used as a test specimen. It was fabricated by using improved spacer grids, and the top and bottom pieces developed in the current project.

Before the test, the top of the test assembly was pressed by 10.92 mm to simulate the BOL hot condition. The 6th grid was clamped to an electromagnetic shaker to apply a forced sinusoidal vibration to the assembly. During the excitation, 5 ~ 50 N were applied discretely and the frequency was increased from 1 to 55 Hz with a uniform speed of 0.01~0.1 Hz/s. The excitation forces

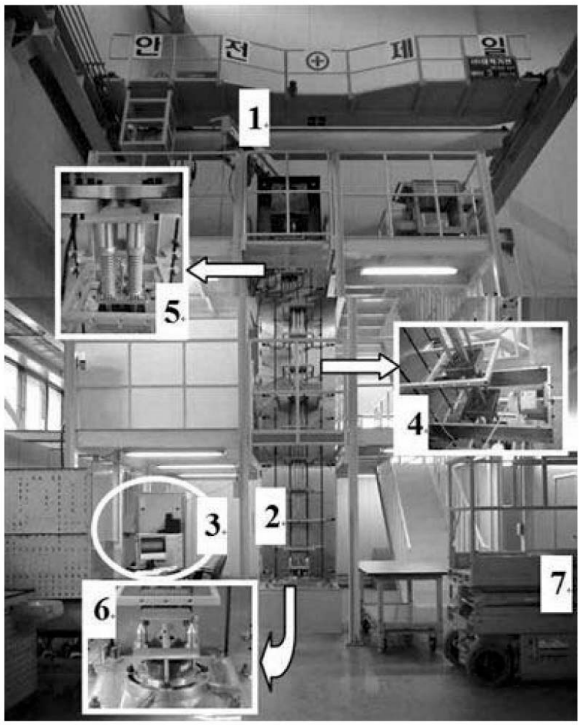

Fig. 24. View of the FAMeCT; 1: Cranes 2: Concrete Column and Steel Bed 3: DAS and PC 4: Shaker (or Loader) and Brackets 5: UCP Simulator 6: LCP Simulator and Rotary Table 7: Self-Propelled Scissors Lift.

and responding vibration amplitudes were amplified and collected in dynamic scanners and a PC. Those signals were analyzed by using the IDEAS T-DAS program.

Figure 25 illustrates the vibration responses along the axial direction of the test assembly, which was acquired during a sine sweep test. It is shown that a resonance occurs as the excitation frequency approaches the natural frequencies of the assembly. The amplitudes at the resonances can provide an overall mode shape of the assembly.

The natural frequencies of the test assembly can be readily obtained from the peaks of the frequency response function without conducting a modal analysis. Table 3 gives the natural frequencies in terms of the excitation forces estimated from the frequency response function.

As illustrated in Fig. 26, mode shapes are determined by normalizing the vibration amplitude at specified locations along the assembly axial direction, which are obtained while exciting the test assembly with the natural frequencies. Since the excitation location (6^{th} grid) was close to the nodal point of the even-numbered modes, the mode shapes of the even-numbered natural frequencies are somewhat distorted. This can be resolved by altering the excitation location other than the 6^{th} grid (e.g., 5^{th} grid).

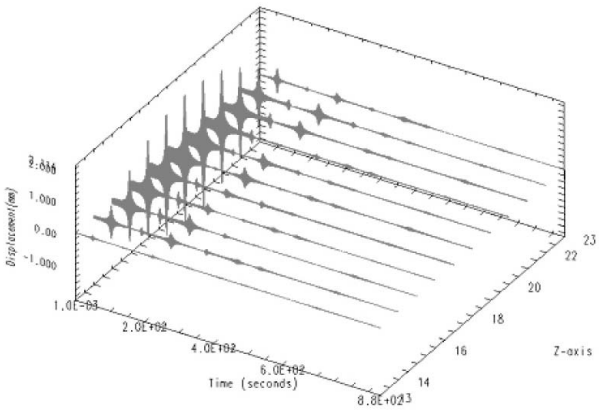

Fig. 25. Vibration Response Time Trace of the Test Fuel Assembly During the Sine Sweep Test (at 5 lbs).

6.1.3 Lateral Bending Stiffness Tests and Results

After the lateral vibration test, the lateral bending stiffness test was implemented with the same test assembly. The lateral load was applied at the 6^{th} grid

Table 3. Natural Frequency of the Test Fuel Assembly According to the Excitation Force

Mode	Excitation Force				
	8.9N	15N	22.2N	30N	44.5N
1	4.53	4.37	4.34	4.25	3.88
2	9.39	9.73	9.35	9.56	9.34
3	14.79	14.62	14.83	14.58	14.76
4	20.74	21.00	20.20	20.90	20.69
5	26.61	26.43	26.10	26.22	26.17
6	30.52	30.29	30.56	30.31	29.97

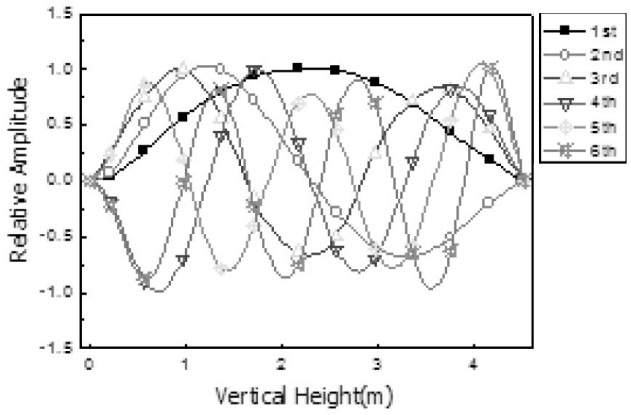

Fig. 26. Normalized Mode Shape of the Test Fuel Assembly

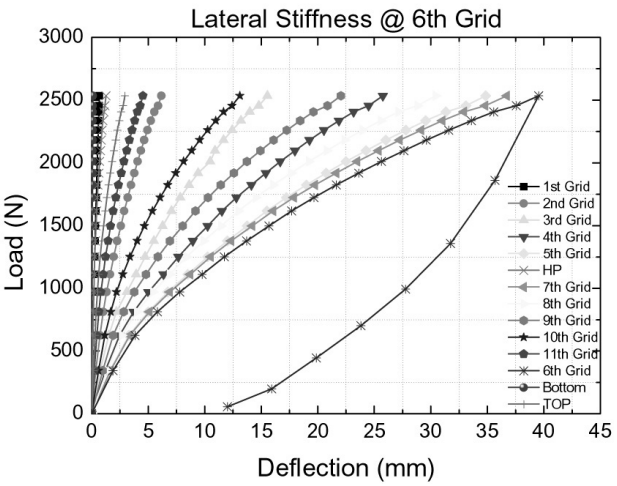

Fig. 27. Lateral Load vs. Deflection Curves From the Lateral Bending Test

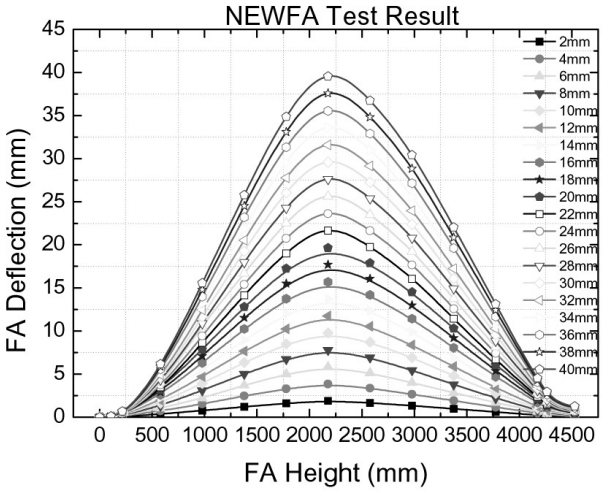

Fig. 28. Fuel Assembly Deflection Shape Obtained From the Lateral Bending Test

location by a screw jack. The deflections were obtained at each spacer grid location by using linear transducers. For this, two transducers were installed at each grid, and the top and bottom end pieces. The applied force was measured simultaneously. The test assembly was deflected by up to 40 mm with an increment of 2 mm. All the signals from the force and displacement transducers were collected and analyzed simultaneously by using static data scanners and StrainSmart®

Figure 27 shows the lateral load vs. deflection at each spacer grid location. It is found that the assembly was deflected in a non-linear manner due to a fuel rod slippage at the grid-to-rod contacts. The fuel assembly did not return to its original location although it was fully unloaded due to the frictional forces of the fuel rods against the grids (i.e., springs/dimples).

Figure 28 shows the deflection shape and magnitude along the axial direction measured at the 6th grid. It shows that the deflection of the upper part (higher than the 6th grid) is a little higher than that of the lower part (lower than the 6th grid). It may be caused by the upper end fitting assembly which is more flexible than the lower end fitting structure.

6.2 Hydraulic Test Loop (HTL)

6.2.1 Fuel Assembly Hydraulic Test Items

Necessary items for fuel assembly hydraulic tests are as listed below.

Pressure loss test: The pressure loss test is conducted to obtain the pressure loss characteristics in a fuel assembly. The measured pressure loss of each component in a fuel assembly is used to determine the

pressure loss coefficient. Those are important input to perform thermal-hydraulic design evaluation and compatibility analysis.

Lift-off test: The lift-off test is to establish the flow rate when the fuel assembly is just lifted off from a simulated lower core plate. The results are used for the major input of a hold down spring design in a fuel assembly.

6.2.2 Description of the HTL

The PWR Hydraulic Test Loop in Fig. 30 consists of a recirculation pump, heat exchangers, electric heaters, a pressurizer, an injection pump, and a virtical test chamber with a full scale single fuel assembly.

The design pressure is 30 bars and the maximum loop flow rate is 500 m^3/hr. The flow rate is changed by increasing or decreasing the pump speed by means of a VVFV (variable voltage variable frequency) connected to the motor of a recirculation pump. Water is heated by an impeller friction heat as well as an electric loop heater. The coolant temperature is controlled by two heaters and a heat exchanger. The loop coolant is de-ionized water.

Fig. 30. View of PWR Hydraulic Test Loop

6.2.3 Hydraulic Tests

The same type of fuel assembly for the mechanical tests was used as a test specimen.

6.2.3.1 Pressure Loss Test

The differential pressure drops over the major components of a fuel assembly were measured span-wisely by several pressure transducers. The locations of the pressure taps are determined to represent a suitable pressure loss of each component such as a bottom end piece, a spacer grid, a fuel rod, a top end piece and a whole fuel assembly.

The pressure loss coefficient was deduced from the pressure loss data by using equitation (1).

$$K_i = \Delta P_i / \frac{1}{2} \rho U^2 \qquad (1)$$

where

K is the pressure loss coefficient,
ΔP is the measured differential pressure loss (Pa),
ρ is the coolant density (kg/m^3),
U is the bundle average coolant velocity (m/s),
and subscript i means each span.

Figure 32 shows the typical pressure loss coefficients of the core and fuel assembly along with the Reynolds number. At a Reynolds number of 20,000 those are 17 and 23, respectively.

6.2.3.2 Lift-off Test

The fuel assembly lift-off happens when the hydraulic force by the coolant flow is equal to or greater than the net assembly weight in the water. This occurrence of a lift-off of the fuel assembly can be detected by a sudden change of the pressure loss in the bottom end piece region due to a flow area change.

The lift-off tests were performed at the coolant temperatures of 65 and 120 °C without a hold down spring. Figure 33 shows the typical results for the cases. The fuel assembly was uplifted at 321 and 341m^3/hr for 65 and 120 °C, respectively. The uplift flow rate varies with the coolant temperature mainly due to a coolant density difference.

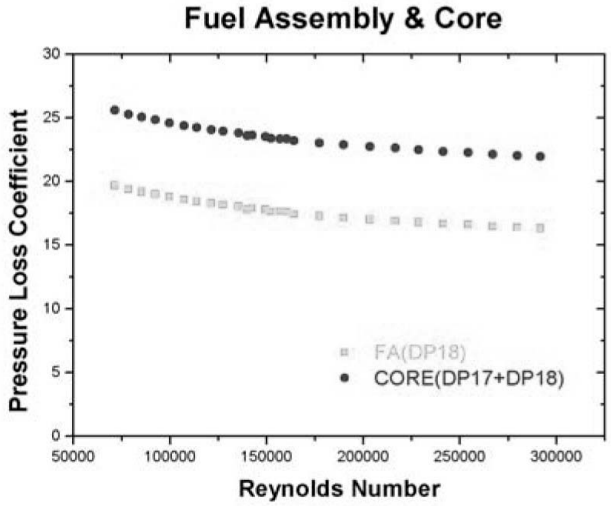

Fig. 32. Pressure Loss Coefficients of Fuel Assembly and Core

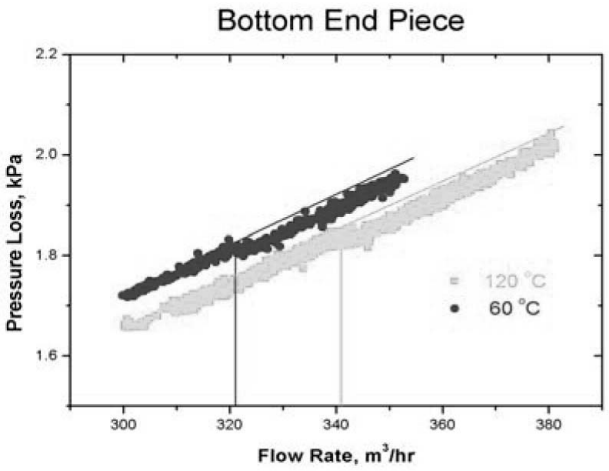

Fig. 33. Lift-Off flow Rate at 65 and 120 °C Coolant Temperature Conditions.

7. CONCLUSION

High burnup fuel technology has been developed in the areas of a cladding, a UO_2 pellet, a spacer grid, and a performance code during the period from 1997 to 2006. The PWR fuel technology is self-reliant and been upgraded to a global level. Specific achievements are summarized below:

1) New cladding tubes were developed which have a high corrosion resistance and a high creep strength. Related technologies were also secured such as an alloy design, heat-treatment, and out-of-pile / in-reactor tests.
2) A sintering process was developed for the fabrication of large grain UO_2 pellets. Uranium oxide seeds are involved in this process as a grain growth promoter. Other special sintering techniques were also developed to fabricate the UO_2 pellet containing W channel
3) Fuel performance analysis code was developed which can accurately deal with high burnup effects such as a rim structure formation and a fission gas release.
4) A spacer grid was developed which can be characterized as theta spring and hybrid mixing vanes. Owing to these features, a rod-supporting ability and a thermal margin are improved significantly. Test facilities were also constructed for mechanical and thermal hydraulic tests of a full size fuel assembly.

REFERENCES

[1] Y.H. Jeong, H.G. Kim, D.J. Kim, B.K. Choi, J.H. Kim, "Influence of Nb concentration in the -matrix on the corrosion behavior of Zr-xNb binary alloys", J. Nucl. Mater., 323, 72 (2003).
[2] H.G. Kim, Y.H. Jeong, T.H. Kim, "Effect of phase, precipitate and Nb-concentration in matrix on corrosion and oxide characteristics of Zr-xNb alloys", J. Nucl. Mater., 317, 1 (2003).
[3] Y.H. Jeong. K.O. Lee, H.G. Kim, "Correlation between microstructure and corrosion behavior of Zr-Nb binary alloys", J. Nucl. Mater., 302, 9 (2002).
[4] J.Y. Park, B.K. Choi, Y.H. Jeong, Y.H. Jung, "Corrosion behavior of Zr alloys with a high Nb content", J. Nucl. Mater., 340, 237 (2005).
[5] H.G. Kim, J.Y. Park, Y.H. Jeong, "Phase boundary of the Zr-rich region in commercial grade Zr-Nb alloys", J. Nucl. Mater., 347, 140 (2005).
[6] V.F. Urbanic, B.D. Warr, A. Manolescu, C.K. Chow, M.W. Shanahan, "Oxidation and deuterium uptake of Zr-2.5Nb pressure tube in CANDU-PHW reactors", Zirconium in the Nuclear Industry, ASTM STP 1023, 20 (1989).
[7] V.F. Urbanic, R.W. Gilbert, "Effect of microstructure on the corrosion of Zr-2.5%Nb alloys", Proc. of IAEA Technical Committee Meeting on Fundamental Aspects of Corrosion on Zirconium Based Alloys in Water Reactor Environments, International Atomic Energy Agency, Vienna, Italy, IWGFPT/34, p.262 (1990).
[8] J.H. Kim, M.H. Lee, B. K. Choi, Y.H. Jeong, "Deformation and thermal quench behavior of HANA cladding in LOCA condition", Proc. of 2005 Water Reactor Fuel Performance Meeting, Kyoto, Japan, Oct. 2-6, p.178 (2005).
[9] J.H. Kim, M.H. Lee, B. K. Choi, Y.H. Jeong, "Deformation of Zircaloy-4 cladding during a LOCA transient up to 1200oC", Nucl. Eng. and Des., 234, 157 (2004).
[10] H. Assmann and H. Bairiot, process and Product Control of Oxide Powder and Pellets for Reactor Fuel Application, in: Guidebook on Quality Control of Water Reactor Fuel, Tech. Report Series No. 221, IAEA, Vienna (1983).
[11] J.A. Turnbull, J. Nucl. Mater. 50 (1974) 62.
[12] Y. Harada, J. Nucl. Mater. 238 (1997) 237.
[13] K.W. Song, K.S. Kim, K.W. Kang, et al., J. Korean Nucl. Soc. 31 (1999) 335.
[14] J.B. Ainscough, F. Rigby, S.C. Osborn, J. Nucl. Mater. 52 (1974) 191.
[15] L. Bourgeois, Ph. Dehaudt, C. Lemaignam, et al., J. Nucl. Mater. 297 (2001) 313.
[16] B.E. Ingleby, K. Hand, in: Fission-Product Behavior in Ceramic Oxide Fuel, Advances in Ceramics vol. 17, I.J. Hastings (eds), Amer. Ceramic Soc., 1986, p. 57.
[17] Y. Harada and S. Doi, J. Nucl. Sci. Technol., 35 (1998) 411.
[18] G.A. Wood and C.P. Perkins, in: Advances in Pellet Technology for Improved Performance at High Burnup, IAEA-TECDOC-1036, IAEA, Vienna, 1998, p. 49.
[19] K.W. Song, K.S. Kim, K.W. Kang, Y.H. Jung, J. Nucl. Mater. 317 (2003) 204.
[20] Y.W. Rhee, K.S. Kim, K.W. Song, Thermochimica Acta 455 (2007) 80.
[21] C.B. Lee, Y.S. Yang, Y.M. Kim, D.H. Kim, J.G. Bang, Y.H. Jung, "High Burnup UO2 Fuel Rod Performance Code INFRA", Proc. of the 2004 International Meeting on LWR Fuel Performance, Orlando, Florida, Sep. 19-22, 2004.
[22] C.B. Lee, Y.S. Yang, "INFRA Code Results of FUMEX-II", IAEA CRP "Improvement of models used for fuel behavior simulation (FUMEX-II), IAEA, Vienna, Dec. 5-8, 2005.
[23] C.B. Lee, D.H. Kim, Y.M. Kim, Y.S. Yang, S.K. Kim, Y.H. Jung, Y.B. Chun, H.S. Seo, E.P. Lee, H.K. Lee, H.M. Kwon. Y.H. Jung, D.K. Min, J.I. Kim, O.H. Kim,

H.D. Chae, "Post-irradiation Examination of High Burnup UO_2 Fuel", Proc. of the 2004 International Meeting on LWR Fuel Performance, Orlando, Florida, Sep. 19-22, 2004.
[24] D. H. Kim et al., "Post-Irradiation Annealing Test of High Burnup UO_2 Fuel", 2005 Water Reactor Fuel Performance Meeting, Kyoto, Japan, Oct. 2-6, 2005.
[25] S. Ravel, et al., "Partitoning of grain boundary and matrix gas inventories: Results obtained using the ADAGIO facility", Fission Gas Behavior in Water Reactor Fuels, Cadarache, France, 2002.
[26] Averty, X. et. al., "Tensile tests on ring specimens machined in M5 cladding irradiated 6 cycles" IRSN 2003/50, 2003.
[27] Daum, R. S. et. al., "On the Embrittlement of Zircaloy-4 Under RIA-Relevant Conditions" Zirconium in the Nuclear Industry : Thirteenth International Symposium, ASTM STP 1423, PA, pp. 702-719, 2002.
[28] K.H. Yoon, K.N. Song, T.H. Chun, D.S. Oh, W.K. In, H.K. Kim, H.S. Kang, and Y.H. Jung, "Spacer Grid for Nuclear Fuel Assemblies with Grid Springs Maintaining Conformal Contact with Fuel Rods and Enlarged Elastic Range," US Patent US 6707872 B2, 2004.
[29] K.H. Yoon, K.N. Song, T.H. Chun, D.S. Oh, W.K. In, H.K. Kim, H.S. Kang, and Y.H. Jung, "Spacer Grid with H-spring for Fuel Rods for Use in Nuclear Reactor Fuel Assemblies," US Patent US 6167105, 2000.
[30] H.S. Kang, K.N. Song, K.H. Yoon, T.H. Chun, D.S. Oh, W.K. In, H.K. Kim, and Y.H. Jung, "Side-slotted Nozzle type Double Sheet Spacer Grid for Nuclear Fuel Assemblies," US Patent US 6744843 B2, 2004.
[31] H.S. Kang, K.N. Song, K.H. Yoon, T.H. Chun, D.S. Oh, W.K. In, H.K. Kim, and Y.H. Jung, "Grid with Nozzle-type Coolant Deflecting Channels for Use in Nuclear Reactor Fuel Assemblies," US Patent US 6130927, 2000.
[32] K.N. Song et al., "Multydisplinary Design of the Spacer Grid Assembly for PWR," IWMDE2006, Japan, 2006.
[33] Frick et al., "Overview on the Development and Implement of Methodologies to Compute Vibration and Wear of Steam Generator Tubes," Symposium on Flow Induced Vibration: Vol. 3, Vibration in Heat Exchanger, pp. 149-161, 1984.
[34] S.H. Lee, J.Y. Kim, and K.N. Song, Design Improvement of an OPT-H Type Nuclear Fuel Rod Support Grid by Using an Axiomatic Design and an Optimization, Journal of Mechanical Science and Technology, Vol. 21, pp.1191-1195, 2007.
[35] C.H. Shin, Y.J. Choo, S.K. Moon, S.Y. Chun, T.H. Chun, CHF Performance of a Hybrid Mixing vane Grid for Nuclear Fuel Bundle, Proc. 2007 Int. LWR Fuel Performance Mtg, San Francisco, Sep. 30-Oct. 3, 2007.
[36] Vishay Measurements Group Inc., 2001, "StrainSmart® User's Manual," CT, USA.
[37] Structural Dynamics Research Corporation, 2002, "I-DEAS Master Series 9.0," OH, USA.